ROYAL SOCIETY
OF CHEMISTRY

PAPER

Check for updates

Build-up shielding-factors, physical, & mechanical properties of Er^{3+} doped borophosphate glasses with varied Bi$_2$O$_3$ content

H. A. Abo-Mosallam,[a] Mostafa I. Abdelglil,[b] Eman E. Bayoumi[c] and Ahmed M. A. El-Seidy ✦[d] *[d]

New Er$_2$O$_3$-doped lithium lead borophosphate with nominal composition 10Li$_2$O–10PbO–20B$_2$O$_3$YEr$_2$O$_3$–XBi$_2$O$_3$-(60-(Y + X))P$_2$O$_5$ (where (X = Y = 0) or (Y = 1 and X = 0/2/4/8 mol%) were successfully synthesized. SEM reveals Bi$_2$O$_3$-induced microstructural evolution in Er-doped phosphate glasses, from homogeneity (0 mol% Bi) to phase separation/cracks (8 mol% Bi), balancing densification and network stability. Mechanical strength was also studied using the Makishima–McKenzie principle. The calculated mechanical parameters showed that doping with Er$_2$O$_3$ instead of P$_2$O$_5$ increased the strength and cohesion of the glass structure. Conversely, replacing the phosphate with Bi$_2$O$_3$ reduced the compactness of the glass network. Py-MLBUF was used to calculate the linear attenuation coefficient, mass attenuation coefficient, half-value layer, tenth-value layer and the atomic interaction cross section for attenuation. Single and double layer exposure and energy absorption buildup factors were examined. Physical properties were investigated depending on the variation in Er$_2$O$_3$ and/or Bi$_2$O$_3$/P$_2$O$_5$ concentrations. The substitution of P$_2$O$_5$ with Er$_2$O$_3$ and/or Bi$_2$O$_3$ enhanced the physical and shielding properties of the prepared glass.

1 Introduction

The worldwide expansion of nuclear power plant development to satisfy energy demands, necessitates addressing the occupational risks associated with ionizing radiation, which can cause significant harm to biological tissues.[1] The energy and kind of radiation determine the extent of damage. Gamma-rays are the most dangerous as they readily penetrate the human body. In order to effectively attenuate ionizing radiation and its huge potential damage, researchers are continuing to improve the features of shield materials. Recently, up to 30% of all studies on radiation shielding materials have focused on glass.[2] The composition, clarity, simplicity of shaping, and resistance to breaking make them superior to traditional concrete in terms of radiation shielding.

Phosphate glass has many good thermal and optical properties, as well as great solubility of rare earth ions. However, one of the main disadvantages of phosphate glass is its poor chemical resistance, which can be greatly improved by adding

B$_2$O.[3,4] The improved properties of borophosphate glass with the addition of B$_2$O$_3$ are due to the coordination numbers in its structure – either BO$_4$ or BO$_3$.[3,4] Glasses based on the borophosphate system have many advantages that allow them to be used in many modern applications, the most important of which are, laser devices, fast ion conduction, solid-state ionic devices, and radiation shielding.[3] On the other hand, the addition of PbO to borophosphate glass has been extensively researched. They discovered that adding PbO was what converted BO$_4$ or BO$_3$ in the glass network. Since both BaO and PbO demonstrated strong ionizing radiation absorption, numerous researchers investigated its potential applications in radiation shielding.[5,6] As a non-traditional network, PbO possesses extraordinary glass properties such as a high density, a big refractive index, a high non-linear optical propensity, and spectacular infrared transmission.[7,8] Because of its greater attenuation, ease of melting, good optical quality, wide composition range, and color center self-relaxation, lead -containing glass has proven to be a wise choice.[7,8]

Heavy metal oxide (HMO) glass, particularly those containing PbO, have low relaxation durations and half-value layers as a result of their high density and effective atomic number, which provides good gamma-ray shielding. Lead glass is found in many medical, laboratory, and nuclear applications, including as windows, storage units, and barriers, because it is transparent and has a high attenuation capacity.[9] The toxicity of lead imposes restrictions on its uses, and ideally we need to

[a]*Glass Research Department, National Research Centre, El-Buhouth St, Dokki, Cairo 12622, Egypt*

[b]*College of Medical Technical, Al-Farahidi University, Baghdad 00964, Iraq*

[c]*Nuclear Materials Authority, P.O. Box 530, El-Maadi, Cairo, Egypt*

[d]*Inorganic Chemistry Department, Advanced Materials Technology & Mineral Resources Research Institute, National Research Center, 33 El-Bohouth St., Dokki, P.O. 12622, Cairo, Egypt. E-mail: am.elseidy@nrc.sci.eg; ahmedmaee2@gmail.com*

limit its use and replace the majority of it with other effective shield oxides such as Bi_2O_3.[10] The high density and atomic number of bismuth make it an efficient attenuator of γ-rays. Bismuth compounds, such bismuth oxide (Bi_2O_3), provide superior mechanical strength and thermal stability in shielding materials. Bismuth is safer since it is non-toxic and eco-friendly, which is important in applications like wearable shielding where toxicity is an issue.[11] Research shows how well it works to enhance radiation shielding when added to glass and polymer composites.[12]

Tiny percentages of different additives have been added to glass matrices to fabricate glass-based radiation shielding materials with unique features. Because of their remarkable chemical, optical, and thermodynamic qualities, rare earth oxides have garnered the most interest from researchers as additives.[13] These elements' high atomic numbers also improve the glass's resistance to high-energy radiation, including gamma and neutron radiation, which makes them desirable for use in nuclear power plants, medical devices, and space technology. Lanthanides specifically, have high cross sections for neutron capture.[14] Additionally, lanthanide-doped glasses have enhanced optical, electrical, chemical, thermal stability, and their magnetic qualities further establish them as essential components for cutting-edge applications like medical devices, sensors, and energy systems.[15] Among the luminous rare-earth ions, the triple erbium ion (Er^{3+}) has garnered the greatest attention because of its advantageous energy level structure.[16] Focusing on Erbium, numerous studies emphasized that the addition of Er_2O_3 to the glass composition improved its ability to absorb different kinds of radiation.[17] In this work, a new series of Er_2O_3-doped lithium lead borophosphate glasses were prepared to investigate the effect of Er_2O_3 and/or Bi_2O_3/P_2O_5 concentration variation on their physical and mechanical of properties. The shielding and buildup factors for single and double layers were also investigated. Increasing the concentrations of Er_2O_3 and/or Bi_2O_3 enhanced the physical and shielding properties of the produced glass.

2 Materials and methods

2.1 Synthesis of glass

Lithium lead erbium doped borophosphate glass with varied Bi_2O_3 with nominal composition $10Li_2O–10PbO–20B_2O_3–YEr_2O_3–XBi_2O_3-(60-(Y+X))P_2O_5$ (where $(X=Y=0)$ or $(Y=1$ and $X=0, 2, 4$ and 8 mol%), see Table 1) were synthesized using the melt-quench method. The compositions of the synthesized vitreous specimens are shown in Table 1. An electronic digital LCD Weighting Balance Scale 0.0001 g (FA1004E) was used to precisely weigh various amounts of high-purity chemical reagents, including Li_2CO_3, PbO, H_3BO_3, Er_2O_3, Bi_2O_3, and $NH_4H_2PO_4$. To make a 40 g batch, the mixture of powders was meticulously weighed according to their chemical compositions. Then, in an agate mortar, we mixed and ground the mixture of powders very gently for 45 minutes. To create a consistent mixture of vitreous specimens, the resultant combinations were heated to 800 °C for 60 minutes, which caused the carbonate and ammonia to thermally break down

Table 1 The elemental fractional abundance and density of the prepared samples

Sample ID	Oxides composition						Density ($g\ cm^3$)
	Li_2O	PbO	B_2O_3	Er_2O_3	Bi_2O_3	P_2O_5	
E_0B_0	10	10	20	0	0	60	2.902
E_1B_0	10	10	20	1	0	59	3.013
E_1B_2	10	10	20	1	2	57	3.123
E_1B_4	10	10	20	1	4	55	3.291
E_1B_8	10	10	20	1	8	51	3.675

into oxides and carbon dioxide. For 90 minutes, the glass batches were placed in alumina crucibles to melt at 1250–1300 °C. Molten amorphous materials were decanted over heated stainless steel molds to produce various-shaped glass samples. To release the strain, the prepared amorphous specimens were annealed for two hours at 400 °C before being allowed to cool to room temperature.

2.2 Experimental techniques

The structural and crystallite sizes of the samples were investigated using X-ray diffraction. The XRD patterns were obtained from an X'pert PRO diffractometer with Cu radiation ($\lambda = 1.542$ Å) at 45 kV and 35 mA over the range $2\theta = 5°–60°$. FTIR spectroscopic analyses were obtained for the prepared nanomotors in order to study the molecular vibration and bonding taking place between atoms in the groups. The KBr disk technique was applied using a Vertex 70 spectrometer (Bruker Optiks, Germany) in the range 4000 and 400 cm^{-1}, with a spectral resolution of 2 cm^{-1} and a scan speed of 2 mm s^{-1}. SEM-EDX analysis was performed using a Prisma E-SEM, (Thermo Fisher Scientific, Waltham, Massachusetts, USA), equipped with an integrated EDX unit (energy-dispersive X-ray spectroscopy).

2.3 Mechanical study

The primary challenge in the Makishima–McKenzie principle is utilizing the following relations to determine the total ionic packing density (V_t) and the total dissociation energy per unit volume (G_t) for the glass system oxides:

$$V_t = \left(\frac{1}{V_m}\right) \sum_i V_i x_i \tag{1}$$

$$G_t = \sum_i G_i x_i \tag{2}$$

where the packing density factor (V_i) and the dissociation energy per unit volume of the supplied glass system oxides (G_i) are represented.[18–20] The synthesized specimens' elastic modulus was designed to theoretically extend the Makishima–McKenzie model.[18–20]

2.4 Density calculations

The density was determined using Archimedes' principle, as expressed in eqn (3),

$$\rho = \frac{W_{air}}{W_{air} - W_{xylene}} \times \rho_{xylene} \tag{3}$$

where ρ represents the density of the glass sample, and (W_{air}) denotes the weight of the glass sample in air. The variable (W_{xylene}) is the weight of the glass sample while immersed in xylene, and ρ_{xylene} is the density of said xylene (Table 1).

2.5 Percentage change

To investigate the change % on going from A value to B value, eqn (4) was used,

$$\% \text{ change} = \frac{(B_{value} - A_{value}) \times 100}{A_{value}}. \tag{4}$$

2.6 Gamma shielding

Py-MLBUF [21,22] was used to calculate the linear attenuation coefficient (LAC), mass attenuation coefficient (MAC), half-value layer (HVL), tenth value layer (TVL), and effective atomic number for attenuation (Z_{eff}). The atomic interaction cross section for attenuation (σ-atomic) and the electron interaction cross section for attenuation (σ-electron) against energy were also investigated. The buildup factors are correction variables that take into consideration the impact of secondary particles in the materials and scattered radiation. The exposure buildup factor (EBF) and energy absorption buildup factor (EABF) were investigated for a single layer, and the double layer buildup factors (DLEABF and DLEBF) were examined for a double layer shield. The combination of double layers was set as AB and BA, with all glass samples as 1st and then as 2nd layer.

The Py-MLBUF platform was validated in detail for 32 materials, including standard, plastics and polymers, pure-compounds, fatty-acids, building-materials.[11,21] Fundamental parameters including atomic weights and gamma-photon cross-sections for the first 92 elements of the periodic table were obtained from NIST – XCOM and XAAMDI – and the standard values of GPF-parameters for 23 elements were obtained from the ANSstandard.[23] The effects of photon scattering while passing through Gamma-ray shielding parameters (GSP) are described by BUF. The online platforms support up to 15 layers, before applying the overestimation-correction in the Py-MLBUF, this led to some errors in the calculation. In the current study only single and double layers were investigated for more accurate results.[24]

The total MAC $(\mu\cdot\rho^{-1})_{Total}$ for the material is the sum of the coefficients of photoelectric absorption $(\mu\cdot\rho^{-1})_{pe}$, Compton scattering $(\mu\cdot\rho^{-1})_{cs}$ and pair production $(\mu\cdot\rho^{-1})_{pp}$ (eqn (5)),[25]

$$(\mu\cdot\rho^{-1})_{Total} = (\mu\cdot\rho^{-1})_{pe} + (\mu\cdot\rho^{-1})_{cs} + (\mu\cdot\rho^{-1})_{pp} \tag{5}$$

where μ is LAC and ρ is the density of the selected sample. The true mass absorption coefficient is given by eqn (6),

$$(\mu\cdot\rho^{-1})_{en} = (\mu\cdot\rho^{-1})_{pe} + (\mu\cdot\rho^{-1})_{cs} + (\mu\cdot\rho^{-1})_{pp} \times \left(\frac{E - 1.02}{E}\right) \tag{6}$$

where E is the incident photon energy. Using eqn (7) Z_{eq} can be interpolation whose ratio $(\mu\cdot\rho^{-1})_{cs}/(\mu\cdot\rho^{-1})_{Total}$ lies in between two successive ratios of elements,

$$Z_{eq} = \frac{Z_1(\log R_2 - \log R) + Z_2(\log R - \log R_1)}{\log R_2 - \log R_1} \tag{7}$$

where Z_1 and Z_2 are the elemental atomic numbers, R_1 and R_2 corresponding to the ratios, respectively, and R is the ratio for the selected material at the specified energy, $R_1 < R < R_2$.

The equivalent atomic numbers are averaged over the 25 incident γ–E and the obtained atomic number is treated as the effective atomic number Z_{eff} of that sample for a given energy range (eqn (8)),

$$Z_{eff} = \sum_{B=0.015}^{15.0} \frac{Z_{eq}}{25}. \tag{8}$$

The buildup factors were calculated according to eqn (9) using GP within the energy spectrum of 0.01515 MeV and up to a penetration depth of 40 mean free paths (mfp)

$$B(E, x) = 1 + \frac{b-1}{K-1}\left(K^X - 1\right) \text{for } K \neq 1 \tag{9}$$

$$B(E, x) = 1 + (b-1)x \text{ for } K = 1. \tag{10}$$

The expression $K(E, x)$ denotes the photon dose multiplication factor, which is determined by eqn (11) for $x \leq 40$ mfp,

$$K(E, x) = Cx^a + d\frac{\tan h\left(\frac{X}{X_K} - 2\right) - \tan h(-2)}{1 - \tan h(-2)} \tag{11}$$

where b is the accumulation factor at 1 mfp, E denotes the energy of the incident photon, and x refers to the distance from the source to the detector within the medium, measured in units of mfp.

DLEABF and DLEBF are required for calculating the buildup factors for double-layered shields (eqn (12) and (13)),

$$B(E, x) = B_2 + \frac{B_1(X_1) - 1}{B_2(X_1) - 1} C(X_2)[xB_2(X_1 + X_2 - B(X_2))] \tag{12}$$

$$C(X_2) = \int \begin{cases} e^{-1.08\beta X_2 + 1.13\beta l(-X_2)}, \text{ HZFLZ,} \\ 0.8l(X_2) + \left(\frac{\gamma}{K}\right)e^{-X_2}, \text{ LZFHZ} \end{cases} \tag{13}$$

where eqn (12) and (13) B(X_1, X_2) refer to DLEBF (or DLEABF) for the double-layered shields with X_1 and X_2 as the mfp of the first and second layer, respectively.

3 Results and discussion

3.1 XRD

The XRD patterns for the selected synthesized samples E_0B_0, E_1B_2, and E_1B_8 were studied to determine the amorphous nature of the prepared samples and to confirm that the formed materials were in a glassy state, as shown in Fig. 1a–d. Deconvolution of the XRD patterns for the selected glass are presented in Fig. 1b–d. The presence of two distinct broad halos with
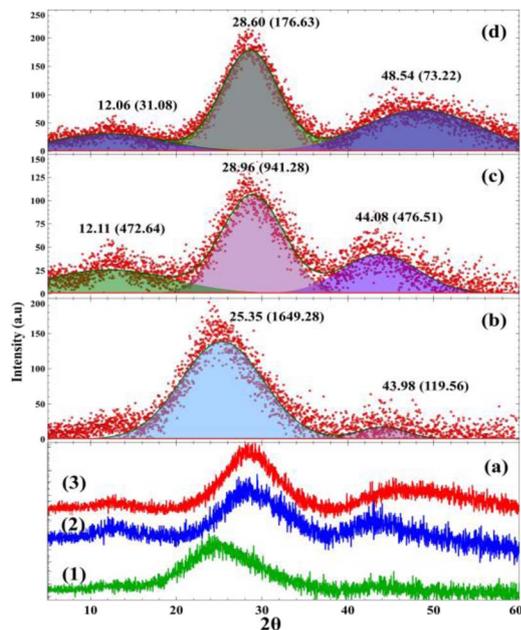
Fig. 1 (a) The XRD patterns of the samples (1) E_0B_0, (2) E_1B_2, and (3) E_1B_8, and the deconvolution XRD of (b) E_0B_0, (c) E_1B_2, (d) E_1B_8.

maxima around 25.35° and 43.98°, in the base glass E_0B_0, indicates phase separation within the glass.[26] The presence of two distinct broad halos, with maxima around 28_0 and 43_0, indicates phase separation within the glass.[26] In the prepared glass, separation can be the result of two interpenetrating borate and phosphate networks. Notably, the primary XRD hump shifts to a higher 2θ angle with the addition and increase of Bi_2O_3 concentration, which corresponds to an increase in glass density. On the other hand, the appearance hump at about 12_0 and increase in the intensity of the hump around 45° with Bi_2O_3/P_2O_5 replacement, can be attributed to the ability of bismuth oxide to enter the glass network as a glass former.

3.2 FTIR

One of the most important aspects of studying glass materials is studying the changes in the internal structure of the glass lattice
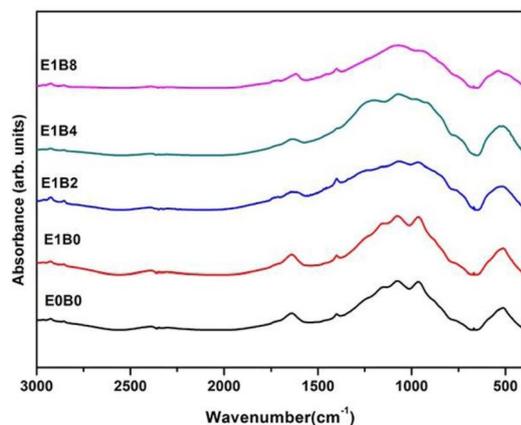

Fig. 2 FTIR spectra of glass samples.

resulting from changes in composition. The changes in the glass lattice can be studied, and accurate and valuable information can be obtained by examining the infrared spectrum FTIR. Fig. 2 shows the FTIR bands of the synthesized glass in the Li_2O–$PbOB_2O_3$–Er_2O_3–Bi_2O_3–P_2O_5 system. It is clear from Fig. 2, that the spectra are concentrated in three main regions: 400–600 cm^{-1} with middle intensity, 600–1500 cm^{-1} with strong intensity, and 1500–1700 cm^{-1}. It is noted from the shape of the FTIR that all bands are sharp bands, which indicates that the prepared materials are glassy materials that do not contain any crystals.[27,28] Since the compositions investigated in this study consist of two main glass formers, namely, B_2O_3 and P_2O_5 in very similar quantities, we expect to observe vibrational modes belonging to both borate and phosphate groups in the IR spectra. In general, bands in the 800–1200 cm^{-1} range are attributed to the B–O stretching vibrations of tetrahedral BO_4 units while bands in the 1200–1500 cm^{-1} region are attributed to the BO stretching vibrations of trigonal BO_3 units.[29] On the other hand, vibrational modes due to the phosphate units are also observed in a similar frequency range so the IR bands belonging to both borate and phosphate groups are expected to overlap in this region which is the reason for the broad bands observed.[29]

The FTIR spectrum of the base glass E_0B_0 specimen shows the different absorbance peaks at 517 cm^{-1}, 669 cm^{-1}, 765 cm^{-1}, 964 cm^{-1}, 1075 cm^{-1}, 1399 cm^{-1}, and 1637 cm^{-1}, as shown in Fig. 2. The absorbance peak at ~1637 cm^{-1} may be attributed to O–H bending vibrations, P–O–H bridge vibration and B–O–H vibrations.[30,31] The appearance of a band at 1399 cm^{-1}, seems more particularly attributed to B–O bonds in the studied glass[32] and BO stretching vibrations in $[BO_3]$ units.[31] The band around 1075 cm^{-1} corresponds to the vibration of stretching of the B–O–B bond of the tetraborate groups of BO_4 (ref. 33) and asymmetric stretching of metaphosphate group $\nu_{as}(PO_3)$.[34] The absorption band at about 964 cm^{-1} is attributed to the asymmetric stretching vibration of PO-P groups linked with the linear metaphosphate chain.[31,35] The band around 765 cm^{-1} corresponds to symmetric stretching vibration ν_{as}(P–O–P).[34,36] The band around 669 cm^{-1} corresponds to bending vibrations of B–O linkages.[36] The band around 520 cm^{-1} is attributed to bending vibrations of O–P–O bonds[29,37] and vibrations due to PO_2- asymmetric modes.[38] The FTIR results show that adding one mole of neodymium did not lead to the appearance of any new peaks, but there was a change in the intensity of the peaks as shown in Fig. 2. Also, the presence and increase intensity of the band at 600 cm^{-1} was due to Bi–O–Bi oscillations of BiO_6 entities for the samples from E_1B_2 to E_1B_8.[38,39]

3.3 SEM-EDX analysis

In-depth SEM analysis of phosphate glass microstructures (Fig. 3) reveals the morphological evolution of raw phosphate glass samples (E_0B_0 to E_1B_8) with varying compositions. The dual-magnification approach (500× and 1000×) allows for a detailed assessment of surface topography, homogeneity, and potential phase separation E_0B_0 (Fig. 3a and b) shows
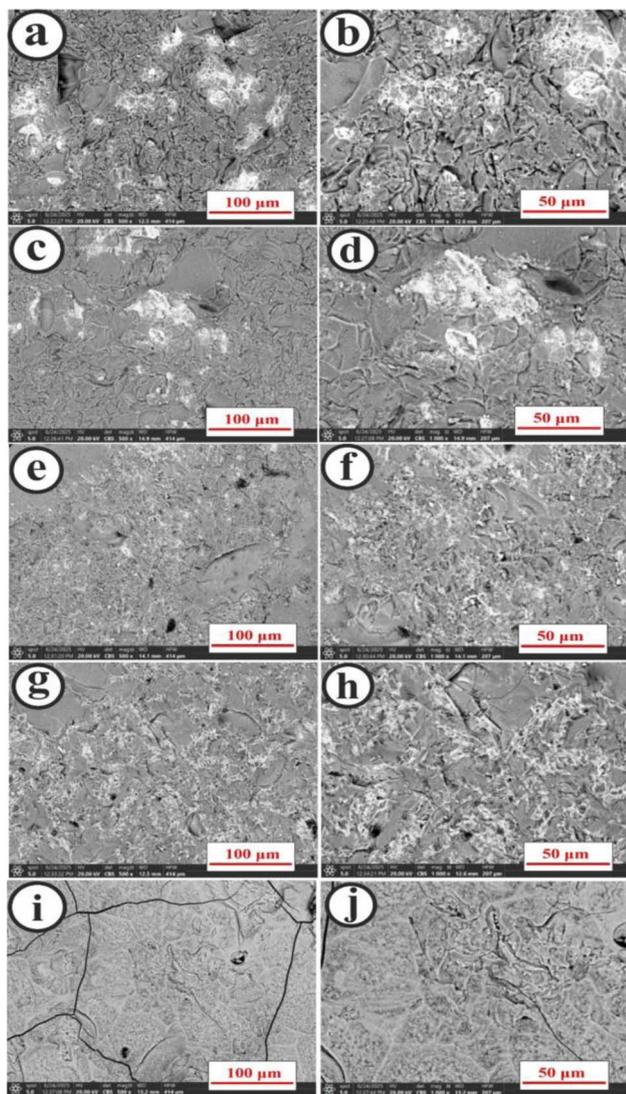

Fig. 3 SEM micrographs of phosphate glass samples: (a and b) E_0B_0, (c and d) E_1B_0, (e and f) E_1B_2, (g and h) E_1B_4, and (i and j) E_1B_8, captured at magnifications of 500× and 1000×, respectively.

a relatively smooth matrix with minimal visible defects, indicating a well-homogenized structure. No phase separation or crystallization is observed, typical of undoped phosphate glass. Minor surface pits and/or scratches likely result from polishing or fracturing during preparation.

Also, SEM microstructures reveal gray matrix regions and bright massive PbO clusters (arrows), indicating higher electron density.[40,41] E_1B_0 (Fig. 3c and d) is similar to E_0B_0, with slight textural changes, and submicron heterogeneity at 1000× (Fig. 3d), suggesting early phase separation from compositional tweaks. E_1B_2 (Fig. 3e and f) exhibits distinct microstructural evolution, including faint grain boundaries or secondary phase clusters. High magnification imaging (at 1000× (Fig. 3f)), reveals potential nucleation sites, indicating Er/Bi oxides incorporation may be destabilizing the glass matrix through crystallization or phase separation mechanisms. E_1B_4 (Fig. 3g and h) shows enhanced phase separation/crystallinity (bright

contrast regions and denser phases) and rougher morphology compared to E_0B_0. Sample E_1B_8 (Fig. 3i and j) shows pronounced heterogeneity at a broader scale of magnification. High magnification (1000×, Fig. j) reveals dopant-induced aggregation and microcracks, while 500× imaging displays bulk striations. These features demonstrate how excessive Bi_2O_3 concentrations compromise glass network stability and structural homogeneity. These microstructural defects may degrade mechanical/optical properties, guiding future compositional optimization. Generally, the SEM analysis (Fig. 3) and chemical composition (Table 1) reveal that increasing Bi_2O_3 content (from 0 to 8 mol%) at the expense of P_2O_5 (from 60 to 51 mol%) enhances glass density (from 2.902 to 3.675 g cm^{-3}) but introduces microstructural heterogeneity (phase separation, cracks, and striations in E_1Bi_8). This trade-off highlights the role of Bi_2O_3 as a network modifier that disrupts the phosphate (P_2O_5) matrix while increasing densification, ultimately compromising structural uniformity in these Er-doped glasses.

EDX analysis (Fig. S1) typically confirms the chemical analysis of the phosphor-borate glass framework for all samples, with dominant P kα (at ~2.02 keV), O kα (at ~0.525 keV), and weak B kα (at ~0.183 keV) signals. Also, Pb, a key modifier, exhibits strong Mα (at ~2.35 keV) and minor Lα (at ~10.55 keV)/ Lβ (at ~12.61 keV) peaks, consistent with its 10 mol% content. Er-doped samples are verified *via* Er Lα (6.95 keV) and Lβ (7.81 keV) in Fig. S1(b–e), while Bi-doped samples, a key modifier (Fig. S1c–e), show characteristic Bi-Mα (at 2.423 keV), poor peaks for Lα (at 10.839/10.731 keV) along with poor peaks for Lβ (at 13.024 keV),[11] further validating dopant incorporation. Notably trace impurities were detected, including a tiny kα signal for C, Si, and Al observed at energies of 0.276, 1.041, and 1.487 keV, respectively;[42] a kα signal for Na (1.740 keV) as well as a secondary Kβ (at 1.07 keV), and N (0.392 keV) were detected in the E_0B_0 sample,[40] likely from precursors or polishing and CO_2 trapping. Li was undetectable by EDX due to equipment limitations (because of the Li-based lens), confirming expected compositional integrity. Moreover, the EDX data reveal three key trends in the glass series (Table 2): (1) phosphate network reorganization, with P dropping sharply from 45 at% (E_0B_0) to 1.4 at% (E_1B_0), then stabilizing at 22–34 at% in doped samples, coupled with increasing O (18.9 to 49.8 at%), indicating network expansion. (2) Successful dopant integration, evidenced by controlled Bi accumulation (1.7 to 7.5 at%), consistent Er (~0.5–0.9 at%), and stable Pb (5–7 at%). (3) Declining C (6.5 to 2.0 wt%) and N (1.8 wt% in E_0B_0) suggest improved processing, though traces of Na/Al/Si (<4 at%) persist. Two anomalies require note: an anomalous Si peak (39.8 at% in E_1B_0), likely from measurement artifacts, and trace Rh (0.5 at% in E_1Bi_8), possibly from precursors or polishing.

3.4 Mechanical study

The Young's modulus of glass defines its ability to withstand changes in length under length-wise tension or compression in the linear elasticity regime. As such, it is a critical engineering property for a large range of applications.[18] Understanding and predicting the compositional dependence of Young's modulus

Table 2 EDX analysis for the E_0B_0, E_1B_0, E_1B_2, E_1B_4, and E_1B_8 samples

Sample Element	E_0B_0 Atomic %	Weight %	E_1B_0 Atomic %	Weight %	E_1B_2 Atomic %	Weight %	E_1B_4 Atomic %	Weight %	E_1B_8 Atomic %	Weight %
B	2.4 ± 0.2	0.7 ± 0.1	2.1 ± 0.2	0.7 ± 0.1	2.6 ± 0.2	0.8 ± 0.1	2.7 ± 0.2	0.7 ± 0.1	1.9 ± 0.1	0.5 ± 0.0
C	18.9 ± 0.5	6.5 ± 0.2	16.8 ± 0.4	6.0 ± 0.1	13.2 ± 0.3	4.6 ± 0.1	10.8 ± 0.3	3.3 ± 0.1	7.6 ± 0.2	2.0 ± 0.1
N	4.4 ± 0.8	1.8 ± 0.3	—	—	—	—	—	—	—	—
O	18.9 ± 0.4	8.6	34.0 ± 0.4	16.2 ± 0.2	41.0 ± 0.5	18.9 ± 0.2	45.9 ± 0.5	18.6 ± 0.2	49.8 ± 0.5	17.6 ± 0.2
Na	0.4 ± 0.1	0.2 ± 0.1	0.3 ± 0.0	0.2 ± 0.1	—	—	—	—	—	—
Al	0.5 ± 0.1	0.4 ± 0.0	0.3 ± 0.0	0.2 ± 0.0	0.1 ± 0.0	0.1 ± 0.0	—	—	0.4 ± 0.0	0.2 ± 0.0
Si	2.7 ± 0.1	2.2 ± 0.1	39.8 ± 0.2	36.7 ± 0.1	1.5 ± 0.2	1.2 ± 0.1	1.1 ± 0.1	0.8 ± 0.0	3.7 ± 0.0	2.3 ± 0.1
P	45.0 ± 0.2	39.8 ± 0.2	1.4 ± 0.0	7.0 ± 0.1	34.1 ± 0.2	30.4 ± 0.2	29.2 ± 0.2	23.0 ± 0.1	22.7 ± 0.2	15.5 ± 0.1
Pb	6.7 ± 0.1	39.8 ± 0.8	5.3 ± 0.1	33.0 ± 0.6	4.9 ± 0.2	29.3 ± 0.9	6.0 ± 0.2	31.7 ± 0.8	5.2 ± 0.2	23.7 ± 0.7
Er	—	—	—	—	0.9 ± 0.1	4.2 ± 0.1	0.5 ± 0.0	2.2 ± 0.1	0.6 ± 0.0	2.2 ± 0.1
Bi	—	—	—	—	1.7 ± 0.1	10.5 ± 0.8	3.7 ± 0.1	19.7 ± 0.7	7.5 ± 0.1	34.7 ± 0.6
Rh	—	—	—	—	—	—	—	—	0.5 ± 0.1	1.2 ± 0.2

is therefore key to accelerating the discovery of novel glass with tailored strength.[43] The theoretically-derived Makishima–Mackenzie (M–M) model expresses the Young's modulus of glass in terms of two determining factors, namely, the interatomic bonding strength (dissociation energy) (G_i) and the ways in which atoms are packed (atomic packing fraction) (V_p).[43] The model calculates Young's modulus ($E_{M–M}$), bulk modulus ($K_{M–M}$), shear modulus ($S_{M–M}$), and longitudinal modulus ($L_{M–M}$) through eqn (14)–(17).[44,45] This simple model offers a clear physical picture to understand the compositional dependence of the stiffness of glass. it provides a simple, physical way to understand how glass composition affects its stiffness, although it often underestimates the actual Young's modulus for many glasses.[43]

$$E_{M–M} = 2V_p G_i \ (\text{GPa}) \quad (14)$$

$$K_{M–M} = 1.2 V_P E_{M–M} \ (\text{GPa}) \quad (15)$$

$$S_{M–M} = \frac{3 E_{M–M}.K_{M–M}}{(9K_{M–M} - E_{M–M})} \ (\text{GPa}) \quad (16)$$

$$L_{M–M} = K_{M–M} + \frac{4}{3} S_{M–M} \ (\text{GPa}) \quad (17)$$

The well-known M–M model was used to calculate the elastic characteristics and Poisson's ratio for investigating the mechanical properties of the synthesized glasses.[18] The packing density parameter (V_t) values were determined to calculate the different elastic parameters such as Young's modulus, E; bulk modulus, B; shear modulus, S; longitudinal modulus, L; and, Poisson's ratio, σ, as summarized in Table 3 and graphically represented in Fig. 4a–c. The elastic parameters for the
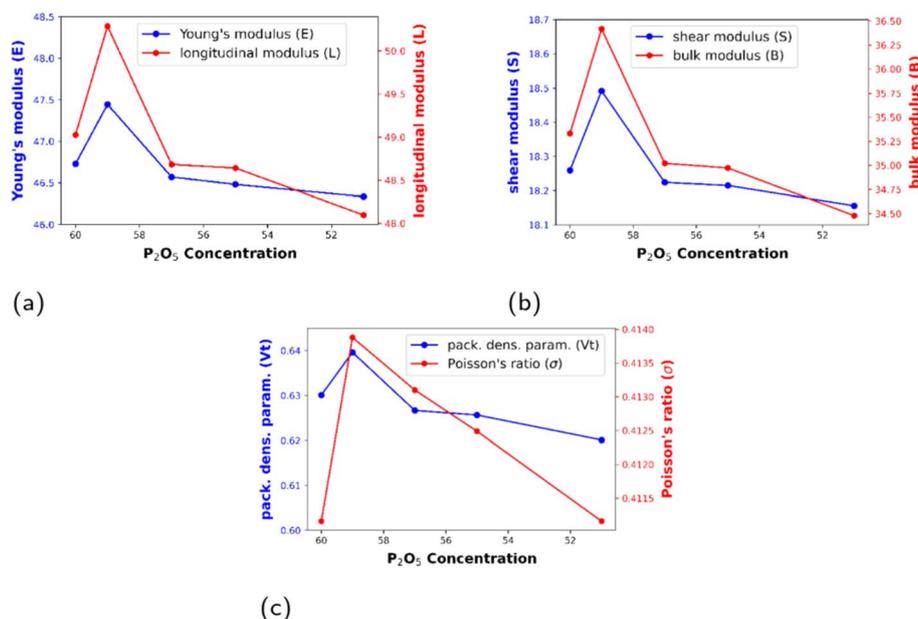

Fig. 4 (a) Young's modulus, longitudinal modulus, (b) shear modulus, bulk modulus, and (c) bulk modulus, and Poisson's ratio *versus* P_2O_5 concentration.

Table 3 Mechanical properties of the prepared glass depending on variation in Er_2O_3, Bi_2O_3, and P_2O_5 concentration

Parameters	E_0B_0	E_1Bi_0	E_1Bi_2	E_1Bi_4	E_1Bi_8
Young's modulus (E)	46.728	47.446	46.57	46.481	46.335
Shear modulus (S)	18.259	18.492	18.224	18.215	18.156
Longitudinal modulus (L)	49.026	50.287	48.682	48.64	48.096
Bulk modulus (B)	35.332	36.418	35.021	34.973	34.479
Packing density parameter (V_t)	0.6301	0.63963	0.62667	0.62566	0.62012
Poisson's ratio (σ)	0.41116	0.41388	0.4131	0.41249	0.41116

prepared vitreous samples were as follows: Young's modulus (E) varied between 47.47 and 46.34 GPa; bulk modulus (B) varied between 36.42 to 34.45 GPa; shear modulus (S) varied between 18.49 to 18.16 GPa; and longitudinal modulus (L) varied between 50.29 and 48.10 Gpa. The bonding strength of the glass network depends largely on the various components that make up the glass system. The mechanical properties result clearly indicates that doping the prepared glass system with 1 mol% Er_2O_3 leads to a significant improvement in the calculated elastic modulus as shown in Fig. 4 and Table 3. The significant increase in mechanical properties upon addition of Er_2O_3 can be attributed to an improvement in the strength of the glass network. Improving the mechanical properties of glass indicates that greater structural rigidity and enhanced resistance to deformation.[46–48] Er^{3+} ions have higher field strength and can clasp non-bridging oxygen in glass structure and increase the roughness and strength of the materials. Previous studies have shown that adding erbium oxide to the glass network leads to stronger bonds between atoms or molecules within the glass network and gradually leads to increased values of elastic characteristics parameters.[49,50] The density, bulk, elastic, and shear modulus of synthesized vitreous materials improved with Er_2O_3 addition, due to the growing bridging oxygen amount in the glass network structure.[49–51] Table 3 and Fig. 4 present the values for the elastic modules parameters for Er_2O_3 doped Li_2O–PbO–B_2O_3–Er_2O_3–P_2O_5 glass samples. One can clearly deem that all elastic moduli parameters decrease as Bi_2O_3 replaces P_2O_5 in the synthesized glass structure. This can be attributed to decreased compactness of the glass structure with incorporation of Bi_2O_3 in the glass network. The infrared spectroscopy
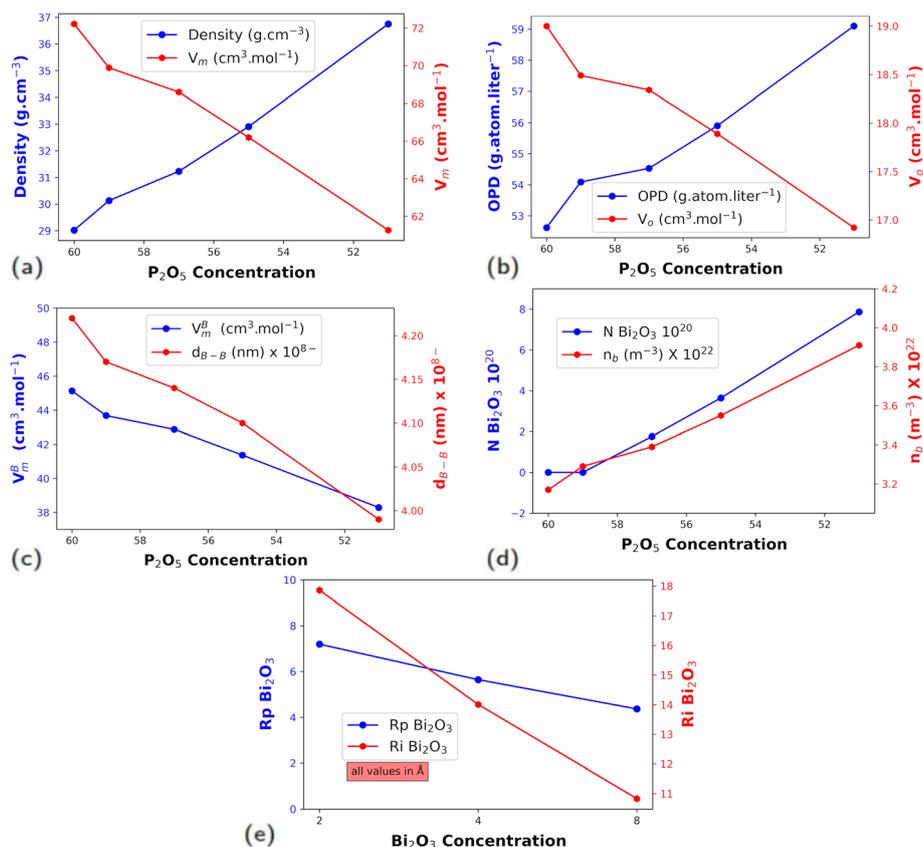

Fig. 5 Effect of Er_2O_3/Bi_2O_3 replacement of P_2O_5 on (a) density, and V_m, (b) OPD, and V_o, (c) V_m^B, and d_{B-B}, (d) N Bi_2O_3, and n_b and (e) R_p Bi_2O_3 and R_i Bi_2O_3.

shows the presence of BiO_6 and PO_3 structural groups and reveals the depolymerization of the phosphate links by the creation of the Bi–O–P groups. The addition of Bi_2O_3 instead of P_2O_5 in glass with the formula $5Ta_2O_5$-xBi_2O_3-$(95-x)P_2O_5$ led to the presence of BiO_6 and PO_3 structural groups and reveals the depolymerization of the phosphate links by the creation of the Bi–O–P groups.[52] The impact of the addition of Bi_2O_3 on the structure of the Li_2O–Na_2O–Nd_2O_3–P_2O_5 glass system was studied.[53,54] ^{31}P MAS NMR results supported the transformation of structural units in the direction from Q^2 to Q^0 with increasing Bi_2O_3 content, attributed to Bi_2O_3 acting as a structure modifier.[53] The results showed that the V_t and σ decrease with increasing Bi_2O_3/P_2O_5 replacement (BiP-R), which confirms the correctness of the calculated mechanical parameters. The relationship between atomic packing density and Poisson's ratio is directly proportional.[55] Decreasing the values of both V_t and σ reflect the decrease in compactness of the vitreous network structure.[56,57]

3.5 Physical study of the prepared glass

Density is regarded as a key property affecting almost all other physical properties of glass.[58,59] The current study investigates the replacement of P_2O_5 with Er_2O_3 (1 mol%) then with Bi_2O_3 (2, 4, and 8 mol%). Table 4 and Fig. 5a–d illustrate the effect on the physical properties of the prepared glass. Doping with 1.00 mol% Er_2O_3 increased the density by 3.82% (from 2.90 to 3.01 g cm^{-3}) which may be due to the density difference between Er_2O_3 (8.64 g cm^{-3}) and P_2O_5 (2.39 g cm^{-3}).[60,61] On doping with Bi_2O_3, E_1B_0 is used as the new base structure for E_1B_2, E_1B_4, and E_1B_8, and hence all change ratios are based on it, since all have the same basic structure which differ only in Bi_2O_3 mol%. The density increased gradually to 3.12 g cm^{-3} (3.65%, 2 mol%) for E_1Bi_2, to 3.29 g cm^{-3} (9.23%, 4 mol%) for E_1Bi_4, and up to 3.68 g cm^{-3} (21.97%, 8 mol%) at E_1Bi_8. This trend may also be explained by the density difference between Bi_2O_3 (8.90 g cm^{-3}) and P_2O_5 (2.39 g cm^{-3}).[9,11] The sample's molar volume (V_m) was calculated using eqn (18):

$$V_m = \frac{\sum x_i M_{wt-i}}{\rho_i} \quad (18)$$

where, x_i = molar fraction and M_{wt-i} = molar mass fraction.

Table 4 Physical properties of the prepared glass depending on variation in Er_2O_3, Bi_2O_3, and P_2O_5 concentration

	E_0B_0	E_1Bi_0	E_1Bi_2	E_1Bi_4	E_1Bi_8
Density (g cm^{-3}) × 10^{-1}	29.02	30.13	31.23	32.91	36.75
V_m (cm^3 mol^{-1}) value	72.21	69.88	68.59	66.19	61.26
OPD (g atom L^{-1})	52.62	54.09	54.53	55.90	59.10
V_o (cm^3 mol^{-1}) value	19.00	18.49	18.34	17.89	16.92
V_m^B (cm^3 mol^{-1})	45.13	43.68	42.87	41.37	38.29
d_{B-B} (nm) × 10^{8-}	4.22	4.17	4.14	4.10	3.99
n_b (m^{-3}) × 10^{22}	3.17	3.29	3.39	3.55	3.91
N (Bi_2O_3) × 10^{20}	0.00	0.00	1.76	3.64	7.87
R_p (Bi_2O_3)	—	—	7.20	5.65	4.3663
R_i (Bi_2O_3)	—	—	17.86	14.01	10.8331
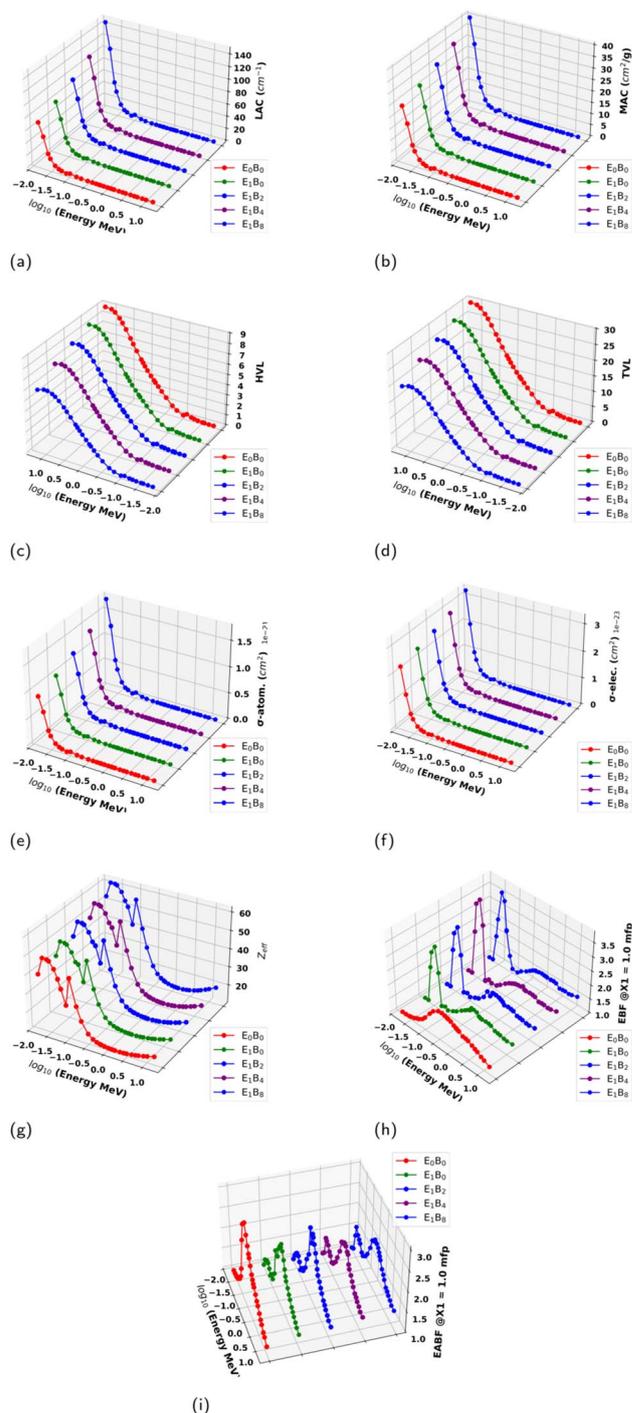
Fig. 6 (a) LAC, (b) total MAC, (c) HVL, (d) TVL, (e) σ-atomic, (f) σ-electron, (g) Z_{eff}, (h) EBF and (i) EABF versus $\log_{10}$ of photon energy of single-layer glass samples. EBF and EABF at selected penetration depth ($X_1 = 1$ mfp).

Table 4 and Fig. 5 show a decrease in V_m by 3.23% (E_0B_0: 72.21, E_1Bi_0: 69.88) due to 1 mol% Er_2O_3/P_2O_5 replacement (ErP-R), while 2 mol% BiP-R led only to −1.85% change. In both Er_2O_3 and Bi_2O_3 the central cations have coordination number (C_{no}) of 6 and even Bi_2O_3 (8.90 g cm^{-3}) is slightly denser than Er_2O_3 (8.64 g cm^{-3}). The higher effect on ErP-R may be due to

Er_2O_3 causing more compression in the basic glass structure. This assumption is also supported by the % change in density (3.82% @ 1 mol% ErP-R and 3.65% 2 mol% BiP-R). The increase of Bi_2O_3 concentration led to a further decrease in V_m values (E_1Bi_4: −5.28%, E_1Bi_8: −12.34%). The decrease in V_m values results from two factors: (i) theoretically, V_m is inversely related to density, which increased with increasing Bi^{3+} concentration, (ii) the replacement of 4-coordinated cation (P in P_2O_5) with 6-coordinated cations (Er^{3+} in Er_2O_3 and Bi^{3+} in Bi_2O_3).[59,60,62] Oxygen packing density (OPD) was calculated using eqn (19):

$$OPD = \frac{c \cdot \rho \cdot 10^3}{M_{wt}} \qquad (19)$$

where, c = the amount of oxygen in the glass, ρ = the density and M_{wt} = sum of molar mass fraction.

After density, OPD is the next most important physical property of glass since it has a direct impact on other properties. Table 4 and Fig. 5b show the OPD values, which show a general increase from 52.62 (E_0B_0) to 59.10 g atom L^{-1} (E_1B_8). The increase in OPD values is strongly related to the increase in density and also the higher C_{no} of Er^{3+} and Er^{3+}, which is 6, compared to that of P^{5+} (4).[59,63,64] The results indicate an optimal value of OPD at E_1B_8 with maximum Er^{3+} and Er^{3+} loading. Other physical parameters were calculated using:

$$V_o = \frac{V_m}{\sum x_i . n_i} \qquad (20)$$

$$V_m^B = \frac{V_{m-i}}{2(1 - X_B)} \qquad (21)$$

$$d_{\langle B-B \rangle} = \left(\frac{V_m^B}{2(1 - X_B)} \right)^{1/3} \qquad (22)$$

$$N = \frac{X_{Cu} \cdot \rho \cdot Na}{M_w} \qquad (23)$$

$$R_P = \frac{1}{2} \left(\frac{\pi}{6N} \right)^{\frac{1}{3}} \qquad (24)$$

$$R_i = \left(\frac{1}{N} \right)^{\frac{1}{3}} \qquad (25)$$

$$n_b = \frac{N_a \cdot \sum x_i n_f}{V_m} \qquad (26)$$

where V_o is the oxygen molar volume, V_m^B is the boron atom molar volume, d_{B-B} is the average boron–boron separation, x_B is the molar fraction of B_2O_3, Na is Avogadro's number (6.0228 × 10^{23} g mol^{-1}), N is the ionic concentration, R_p is the polaron

Table 5 MAC and LAC for prepared glass calculated using Py-MLBUF

Energy MeV	Total MAC ($cm^2 g^{-1}$)					LAC 1/cm				
	E_0B_0	E_1B_0	E_1B_2	E_1B_4	E_1B_8	E_0B_0	E_1B_0	E_1B_2	E_1B_4	E_1B_8
0.0150	24.473	27.045	30.392	33.8	40.138	71.02	81.487	94.913	111.24	147.51
0.0200	17.333	18.434	21.114	23.821	28.877	50.301	55.543	65.94	78.396	106.12
0.0263	8.4757	9.0054	10.325	11.658	14.148	24.597	27.133	32.246	38.367	51.994
0.0300	6.0663	6.4409	7.3868	8.3419	10.126	17.604	19.406	23.069	27.453	37.214
0.0400	2.9148	3.0879	3.5354	3.9871	4.8311	8.4588	9.3038	11.041	13.121	17.754
0.0500	1.6792	1.7741	2.0233	2.2748	2.7447	4.873	5.3454	6.3188	7.4862	10.087
0.0595	1.1104	1.4783	1.626	1.7824	2.0674	3.2223	4.4541	5.078	5.8658	7.5977
0.0600	1.0907	1.4511	1.5958	1.7489	2.0281	3.1651	4.3721	4.9836	5.7557	7.4532
0.0800	0.58418	0.75374	0.8214	0.89305	1.0236	1.6953	2.271	2.5652	2.939	3.7618
0.1000	1.1148	1.1941	1.3662	1.5403	1.8652	3.2351	3.5978	4.2667	5.069	6.8544
0.1500	0.46894	0.4949	0.55502	0.61577	0.72921	1.3609	1.4911	1.7333	2.0265	2.6798
0.2000	0.27787	0.2895	0.31765	0.34608	0.39918	0.80637	0.87225	0.99202	1.1389	1.467
0.3000	0.15838	0.16207	0.17169	0.1814	0.19955	0.45963	0.48831	0.53619	0.597	0.73334
0.4000	0.11879	0.12037	0.12486	0.12939	0.13785	0.34473	0.36268	0.38995	0.42583	0.50661
0.5000	0.099381	0.10017	0.10264	0.10513	0.10979	0.2884	0.3018	0.32054	0.34599	0.40347
0.6000	0.087544	0.087959	0.08946	0.09097	0.093794	0.25405	0.26502	0.27938	0.29938	0.34469
0.6620	0.082131	0.082411	0.083563	0.084722	0.086889	0.23835	0.2483	0.26097	0.27882	0.31932
0.8000	0.073156	0.073259	0.073903	0.07455	0.075761	0.2123	0.22073	0.2308	0.24535	0.27842
1.0000	0.064214	0.064199	0.064497	0.064795	0.065352	0.18635	0.19343	0.20142	0.21324	0.24017
1.1730	0.058615	0.058554	0.058705	0.058855	0.059135	0.1701	0.17642	0.18334	0.19369	0.21732
1.3330	0.054606	0.054533	0.054621	0.054706	0.054866	0.15847	0.16431	0.17058	0.18004	0.20163
1.5000	0.051297	0.051224	0.051283	0.051341	0.051449	0.14886	0.15434	0.16016	0.16896	0.18908
2.0000	0.044397	0.044366	0.044448	0.044529	0.044681	0.12884	0.13367	0.13881	0.14655	0.1642
2.5060	0.039952	0.039979	0.040125	0.040272	0.040545	0.11594	0.12046	0.12531	0.13253	0.149
3.0000	0.03695	0.037033	0.037249	0.037466	0.03787	0.10723	0.11158	0.11633	0.1233	0.13917
4.0000	0.033045	0.033229	0.033572	0.033921	0.034569	0.095896	0.10012	0.10485	0.11163	0.12704
5.0000	0.030724	0.030993	0.031449	0.031912	0.032773	0.089162	0.093383	0.098216	0.10502	0.12044
6.0000	0.02926	0.029601	0.030154	0.030716	0.031762	0.084912	0.089188	0.094172	0.10109	0.11673
8.0000	0.027673	0.028132	0.028848	0.029576	0.03093	0.080306	0.084762	0.090093	0.097334	0.11367
10.0000	0.026991	0.027547	0.028398	0.029262	0.03087	0.078328	0.083	0.088686	0.096302	0.11345
15.0000	0.026777	0.027516	0.028629	0.02976	0.031865	0.077707	0.082907	0.089409	0.097941	0.1171

radius, R_i is the inter-ionic distance, and n_b is the bonds per unit volume.

The V_o values (Table 4 and Fig. 5b) show the exact same behavior as V_m, decreasing from 19.00 (E_0B_0) to 16.92 cm^3 mol^{-1} (E_1B_8) which depends mainly on the increase in densities of current glass and the replacement of a cation with lower C_{no} (P^{5+}: 4) with ones having higher C_{no} (Er^{3+} and Er^{3+}: 6). The decrease in both V_o and V_m indicate a compression in the glass structural network which in turns explain the decrease in $d_{\langle B-B \rangle}$ and V_m^B values (Table 4 and Fig. 5c). The value of N, R_p and R_i were calculated depending on the variation of Bi_2O_3 concentrations as can be seen in Table 4 and Fig. 5d and e. The values of N agree with the proposed composition starting at 0.00 for E_0B_0 and E_1Bi_0 (no Bi_2O_3) then increasing from 1.76×10^{20} (E_1Bi_2) to maximum value of 7.87×10^{20} at E_1Bi_8. As expected, the values of both R_p and R_i decreased as the concentration of Bi_2O_3 increases. The values of n_b increased on doping from 3.17×10^{22} (E_0B_0) to 3.91×10^{22} m^{-3} (E_1B_8), as the value of n_b depends mainly on C_{no}, the d_{B-B} and OPD values also increased as n_b increased.

3.6 Shielding properties

The LAC, MAC, HVL, TVL and Z_{eff} for all prepared glasses were calculated using Py-MLBUF. The investigations were performed in the energy range 0.015 to 15 MeV (Tables 5 and 6, Fig. 6). In the current study, the following effects were studied. First: 1 mol% Er_2O_3/P_2O_5 replacement on the basic glass structure. The % change in E_1B_0 are with respect to E_0B_0. Second: the effect of 2–8 mol% Bi_2O_3/P_2O_5 replacement on the updated E_1B_0 structure. The % change in other glass samples (E_1B_2, E_1B_4, and E_1B_8) are with respect to E_1B_0. The values of LAC of all glass samples decreased with γ_E increase, showing the maximum values (71.02–147.51 cm^{-1}) @ 0.015 eV. This behavior is also known for most materials.[11,65,66] As γ_E increases, the dominant interaction mechanism changes from photoelectric absorption to Compton scattering.[11,65] Doping glass samples led to an increase in LAC values. The maximum increase was found at minimum γ_E (0.0150 Me V, E_1B_0: 14.74%, E_1B_2: 16.48%, E_1B_4: 36.51%, E_1B_8: 81.02%). The gradual increase of LAC with doping with Er_2O_3 and Bi_2O_3 indicates an improvement in the shielding properties of the glass due to the increase in density.

The total MAC is the sum of coefficients as represented in eqn (27). In the current study, MAC and both σ-atomic and σ-electronic (atomic and electronic cross-sections) generally decrease with increasing energy. At low-energy range, the photoelectric effect is the dominant interaction, where the gamma photon is absorbed by an atom, causing the ejection of a tightly bound electron. The probability of this interaction

Table 6 Z_{eff}, HVL, and TVL for prepared glass calculated using PyMLBUF

| Energy MeV	Z_{eff}					HVL cm					TVL cm				
	E_0B_0	E_1B_0	E_1B_2	E_1B_4	E_1B_8	E_0B_0	E_1B_0	E_1B_2	E_1B_4	E_1B_8	E_0B_0	E_1B_0	E_1B_2	E_1B_4	E_1B_8
0.0150	39.8963	42.1217	45.4244	48.5088	53.6555	0.0098	0.0085	0.0073	0.0062	0.0047	0.0324	0.0283	0.0243	0.0207	0.0156
0.0200	49.239	50.5793	54.0244	57.0542	61.7956	0.0138	0.0125	0.0105	0.0088	0.0065	0.0458	0.0415	0.0349	0.0294	0.0217
0.0263	49.1551	50.476	53.9303	56.964	61.7038	0.0282	0.0255	0.0215	0.0181	0.0133	0.0936	0.0849	0.0714	0.06	0.0443
0.0300	48.5424	49.8703	53.3455	56.4032	61.1902	0.0394	0.0357	0.03	0.0252	0.0186	0.1308	0.1187	0.0998	0.0839	0.0619
0.0400	45.103	46.491	50.0235	53.1789	58.203	0.0819	0.0745	0.0628	0.0528	0.039	0.2722	0.2475	0.2085	0.1755	0.1297
0.0500	40.387	41.818	45.3318	48.5422	53.7906	0.1422	0.1297	0.1097	0.0926	0.0687	0.4725	0.4308	0.3644	0.3076	0.2283
0.0595	35.7334	41.035	43.7838	46.459	50.9788	0.2151	0.1556	0.1365	0.1182	0.0912	0.7146	0.517	0.4534	0.3925	0.3031
0.0600	35.5481	40.8456	43.5902	46.2638	50.7853	0.219	0.1585	0.1391	0.1204	0.093	0.7275	0.5267	0.462	0.4001	0.3089
0.0800	27.5681	32.3352	34.7824	37.2582	41.6361	0.4089	0.3052	0.2702	0.2358	0.1843	1.3582	1.0139	0.8976	0.7835	0.6121
0.1000	42.6672	44.237	47.7334	50.8833	55.9334	0.2143	0.1927	0.1625	0.1367	0.1011	0.7117	0.64	0.5397	0.4542	0.3359
0.1500	28.6258	30.0166	32.9532	35.8018	40.8122	0.5093	0.4648	0.3999	0.342	0.2587	1.692	1.5442	1.3284	1.1362	0.8592
0.2000	21.3812	22.4207	24.5833	26.771	30.8445	0.8596	0.7947	0.6987	0.6086	0.4725	2.8555	2.6398	2.3211	2.0217	1.5696
0.3000	15.5289	16.1572	17.4056	18.7159	21.2849	1.5081	1.4195	1.2927	1.1611	0.9452	5.0097	4.7154	4.2943	3.857	3.1399
0.4000	13.4548	13.9124	14.7688	15.6806	17.5032	2.0107	1.9112	1.7775	1.6278	1.3682	6.6794	6.3487	5.9049	5.4073	4.5451
0.5000	12.5132	12.8897	13.5562	14.2709	15.7121	2.4034	2.2967	2.1624	2.0034	1.718	7.9839	7.6294	7.1834	6.6551	5.707
0.6000	12.0136	12.3466	12.9085	13.5137	14.7395	2.7284	2.6154	2.481	2.3152	2.0109	9.0634	8.6883	8.2417	7.6911	6.6801
0.6620	11.8066	12.1217	12.6428	13.2048	14.3452	2.9082	2.7915	2.6561	2.486	2.1707	9.6607	9.2732	8.8232	8.2583	7.211
0.8000	11.5176	11.807	12.2632	12.7568	13.7608	3.265	3.1403	3.0032	2.8252	2.4896	10.846	10.4318	9.9765	9.3851	8.2702
1.0000	11.2842	11.5531	11.9588	12.3988	13.2957	3.7196	3.5834	3.4412	3.2506	2.8861	12.3564	11.9039	11.4315	10.7981	9.5873
1.1730	11.1764	11.4356	11.817	12.2312	13.0762	4.0749	3.9289	3.7807	3.5786	3.1895	13.5366	13.0514	12.5593	11.8879	10.5953
1.3330	11.1202	11.3755	11.7454	12.1474	12.9675	4.3741	4.2186	4.0635	3.85	3.4377	14.5305	14.0137	13.4985	12.7895	11.4197
1.5000	11.1027	11.3568	11.7218	12.1186	12.9284	4.6562	4.4911	4.3279	4.1024	3.666	15.4677	14.9192	14.377	13.6278	12.1781
2.0000	11.154	11.4161	11.7898	12.1962	13.025	5.3799	5.1853	4.9935	4.7299	4.2213	17.8716	17.2253	16.5879	15.7124	14.0228
2.5060	11.2832	11.5612	11.9577	12.3884	13.2662	5.9785	5.7543	5.5315	5.23	4.6519	19.86	19.1155	18.3751	17.3736	15.4534
3.0000	11.4238	11.72	12.1437	12.6034	13.5396	6.4641	6.212	5.9586	5.6216	4.9804	21.4733	20.6359	19.794	18.6747	16.5447
4.0000	11.7492	12.0856	12.5691	13.0928	14.1564	7.2281	6.9233	6.611	6.2091	5.456	24.0114	22.9988	21.9614	20.6262	18.1245
5.0000	12.0818	12.4586	13.0026	13.5904	14.7818	7.774	7.4226	7.0573	6.6	5.7551	25.8247	24.6573	23.444	21.9247	19.1181
6.0000	12.4058	12.8208	13.4228	14.0722	15.385	8.1631	7.7718	7.3604	6.8569	5.9382	27.1172	25.8172	24.4507	22.778	19.7264
8.0000	13.004	13.4883	14.1952	14.9551	16.4847	8.6313	8.1776	7.6937	7.1213	6.0981	28.6727	27.1653	25.5579	23.6566	20.2575
10.0000	13.5306	14.0746	14.872	15.7267	17.4405	8.8492	8.3512	7.8158	7.1977	6.1098	29.3965	27.7422	25.9634	23.9101	20.2963
15.0000	14.5722	15.2302	16.202	17.2379	19.2993	8.92	8.3605	7.7526	7.0772	5.9191	29.6317	27.7731	25.7535	23.5099	19.6629

Paper
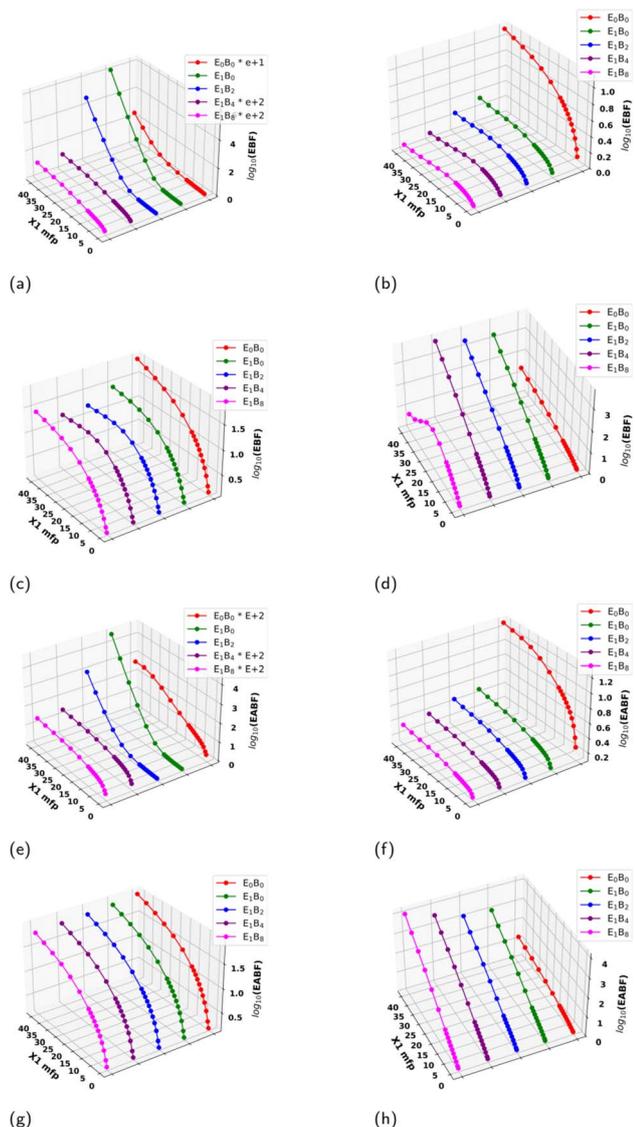
Fig. 7 Log_{10} of EBF at selected photon energies of (a) 0.015, (b) 0.15, (c) 1.5, and (d) 15 MeV and EABF at selected photon energies of (e) 0.015, (f) 0.15, (g) 1.5, and (h) 15 MeV, *versus* penetration depth.

decreases rapidly with increasing γ_E. At mid energy, Compton scattering is dominant, causing scattering of loosely bound outer-shell electrons. Compton scattering probability also decreases with increasing γ_E. At high energy, pair production becomes the dominant interaction which in some cases leads to an increase in the total MAC with materials with high atomic number, this was not applied in the current study. At 0.0150 MeV the changes due to M_2O_3/P_2O_5 replacements were: 10.51% (E_1B_0), 12.38% (E_1B_2), 24.98% (E_1B_4), 48.41% (E_1B_8) in MAC; 13.27% (E_1B_0), 15.99% (E_1B_2), 33.38% (E_1B_4), 69.06% (E_1B_8) in σ-atomic; and 7.28% (E_1B_0), 7.56% (E_1B_2), 15.82% (E_1B_4), 32.71% (E_1B_8) in σ-electronic. The ErBiP-R have a higher impact on the values of the current parameters, which may be summarized as: 24.19% (E_1B_2), 38.11% (E_1B_4), 64.01% (E_1B_8) in MAC; 31.38% (E_1B_2), 51.08% (E_1B_4), 91.49% (E_1B_8) in σ-atomic;

and 15.39% (E_1B_2), 24.25% (E_1B_4), 42.38% (E_1B_8) in σ-electronic.

$$\text{Total MAC}\left(\frac{\mu}{\rho}\right) = \left(\frac{\mu}{\rho}\right)_{\text{photoelectric}} + \left(\frac{\mu}{\rho}\right)_{\text{Compton}} + \left(\frac{\mu}{\rho}\right)_{\text{pair production}} \quad (27)$$

TVL and HVL increase with energy γ_E, since increased thickness shields are necessary for higher-energy radiation. The decrease of TVL and HVL values with doping indicates that a smaller thickness is required which further supports the improvement of shielding properties with doping. 1 mol% ErP-R showed the maximum difference (TVL: −27.66%, HVL: −27.65) @ $\gamma_E = 0.0595$ MeV, while 2 mol% (TVL: −16.00%, HVL: −15.92%), 4 mol% (TVL: −29.60%, HVL: −29.32%), and 8 mol% (TVL: −48.00%, HVL: 47.85%). BiP-R mol% showed a maximum difference @ $\gamma_E = 0.0200$, and 0.0300 MeV, for TVL and HVL, respectively. Z_{eq} is higher at low γ_E since it mainly depends on the photoelectric absorption effect (which is proportional to Z^5), it then decreases gradually as Compton scattering becomes more dominant. For the latter, the effective cross-section is less dependent on Z, which will lead to decreasing Z_{eq} values. ErP-R, BiP-R, and ErBiPR caused an increase in their values with some exceptions: 1 mol% ErP-R showed a maximum difference (104.47%) @ $\gamma_E = 0.0150$ MeV; 2 mol% BiP-R showed irregular behavior with maximum decrease (−19.92%) @ $\gamma_E = 1.1730$ MeV and maximum increase (9.18%) @ 0.1000 MeV; 4 mol% BiP-R showed only one decrease (−12.19%) @ $\gamma_E = 1.1730$ MeV and a maximum change (51.64%) @ $\gamma_E = 0.0600$ MeV; 8 mol% BiP-R showed
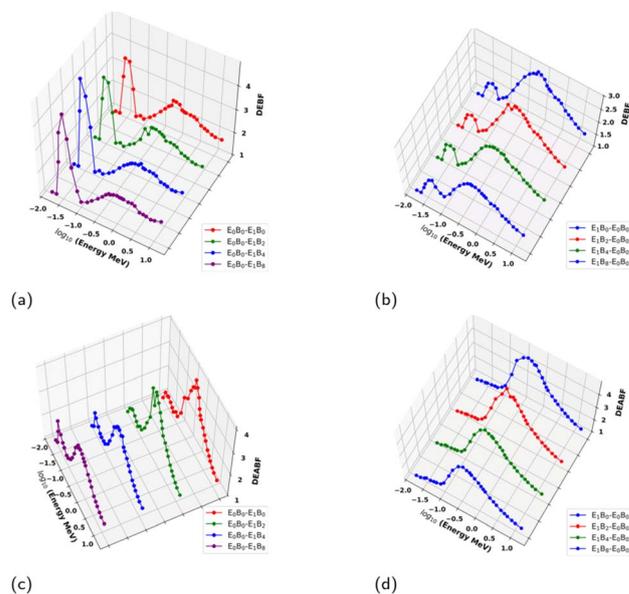

Fig. 8 Factors of DLEBF ((a) and (b)), and DLEABF ((c) and (d)) of double layers at selected penetration depth ($X_1 = X_2 = 1$ mfp) *versus* $\log_{10}$ of photon energy. Here, X_1 and X_2 indicate the penetration depth of the first and second layer, respectively. In (a) and (c) E_0B_0 is the 1st layer while in (b) and (d) it is the 2nd layer.

a maximum change (70.27%) @ 0.0600 MeV. ErBiP-R showed maximum values @ $\gamma_E = 0.5000$ MeV (E_1B_2: 125.80%, E_1B_4: 146.85%) and @ $\gamma_E = 1.1730$ MeV (E_1B_8: 168.09%).

The buildup factor is a measure of how much the radiation dose increases due to scattered radiation. For a single layer, EABF and EBF were calculated at 1 mfp (Fig. 6 h and i) and in the 1.00 to 40.00 mfp range at selected photon energies of $\gamma_E = 0.0150, 0.1500, 1.5000,$ and 15.0000 MeV (Fig. 7a–h). These factors are vital in the correction of the attenuation calculation by taking into account the secondary gamma ray emission.[11] The values of EBF are greater than 1 which indicates that

scattered photons contribute to the total exposure. E_0B_0 showed one peak while the rest of the samples showed two peaks. 1 mol% ErP-R showed a very sharp change (EBF: 190.30% @ 0.04 MeV, EABF: 26.93% @ 0.03 MeV). The same behavior was noted for 2–8 mol% BiP-R (EBF: 223.82–272.59% @ 0.04 MeV, EABF: 31.35–68.63% @ 0.03–0.06 MeV). Which indicates that doping increases the contribution of scattered photons to the total exposure. To investigate the use of the double layer, the following sequence was assumed: DLE0 (E_0B_0 as the 1st layer), and DLE1 (E_0B_0 as the 2nd layer). At penetration depths $X_1 = X_2 = 1$, DLEBF and DLEABF were calculated for all samples (Fig. 8a–d). DLE1 shows lower values than DLE0 which indicates higher effective radiation absorption.

The double layer, DLEABF and DLEBF were calculated at 1 mfp and X_2 in the 1.00 to 40.00 mfp range, at selected photon energies of $\gamma_E = 0.0150, 0.1500, 1.5000,$ and 15.0000 MeV (Fig. 9a–h). Its value increases with increasing X_2, showing the highest values at 40.00 mfp. The values of DLEBF and DLEABF have very complex behavior with respect to composition at the selected γ_E: (i) @ $\gamma_E = 0.0150$ MeV: (a) DLEBF: E_0B_0–E_1B_0 > E_0B_0–E_1B_2 > E_1B_4–E_0B_0 > E_1B_8–E_0B_0 > E_1B_2–E_0B_0 > E_1B_0–E_0B_0 > E_0B_0–E_1B_8 > E_0B_0–E_1B_4. (b) DLEABF: E_0B_0–E_1B_0 > E_0B_0–E_1B_2 > E_1B_0–E_0B_0 = E_1B_2–E_0B_0 = E_1B_4–E_0B_0 = E_1B_8–E_0B_0 > E_0B_0–E_1B_4 = E_0B_0–E_1B_8. (ii) @ $\gamma_E = 0.1500$ MeV: (a) DLEBF: E_1B_0–E_0B_0 > E_1B_2–E_0B_0 > E_1B_4–E_0B_0 > E_1B_8–E_0B_0 > E_0B_0–E_1B_0 > E_0B_0–E_1B_2 > E_0B_0–E_1B_4 > E_0B_0–E_1B_8. (b) DLEABF: E_1B_0–E_0B_0 > E_1B_4–E_0B_0 > E_1B_2–E_0B_0 > E_1B_8–E_0B_0 > E_0B_0–E_1B_0 > E_0B_0–E_1B_2 > E_0B_0–E_1B_4 > E_0B_0–E_1B_8. (iii) @ $\gamma_E = 1.5000$ MeV: (a) DLEBF: E_1B_4–E_0B_0 > E_1B_2–E_0B_0 > E_1B_0–E_0B_0 > E_1B_8–E_0B_0 > E_0B_0–E_1B_0 > E_0B_0–E_1B_8 > E_0B_0–E_1B_2 > E_0B_0–E_1B_4. (b) DLEABF: E_1B_8–E_0B_0 > E_1B_4–E_0B_0 > E_1B_2–E_0B_0 > E_1B_0–E_0B_0 > E_0B_0–E_1B_0 > E_0B_0–E_1B_2 > E_0B_0–E_1B_4 > E_0B_0–E_1B_8. (iv) @ $\gamma_E = 15.0000$ MeV: (a) DLEBF: E_0B_0–E_1B_4 > E_0B_0–E_1B_2 > E_0B_0–E_1B_0 > E_1B_8–E_0B_0 > E_1B_0–E_0B_0 > E_1B_2–E_0B_0 > E_1B_4–E_0B_0 > E_0B_0–E_1B_8. (b) DLEABF: E_0B_0–E_1B_8 > E_0B_0–E_1B_4 > E_0B_0–E_1B_2 > E_0B_0–E_1B_0 > E_1B_0–E_0B_0 > E_1B_2–E_0B_0 > E_1B_4–E_0B_0 > E_1B_8–E_0B_0.

4 Conclusion

This study systematically examined the influence of substituting P_2O_5 with Er_2O_3 and Bi_2O_3 on the structural, mechanical, and γ-ray shielding properties of lithium-lead borophosphate glasses. EDX analysis confirmed the homogeneous incorporation of Er and Bi within the phosphate framework. The incorporation of Er_2O_3 significantly enhanced the rigidity and connectivity of the glass network, reflected by increases in the Young's and bulk moduli from 46.73 to 47.45 GPa and from 35.33 to 36.42 GPa, respectively. This improvement is attributed to the stronger bonding environment and the higher coordination number ($C_{no} = 6$) of Er^{3+} compared to P^{5+} ($C_{no} = 4$). In contrast, Bi_2O_3 addition generated non-bridging oxygen that slightly depolymerized the phosphate network; however, its high atomic mass and density (raising ρ from 3.013 to 3.675 g cm^{-3}) considerably enhanced the LAC and MAC, especially at low photon energies (0.015 MeV). The combined Er_2O_3/Bi_2O_3 substitution reduced molar (V_m) and oxide (V_o) volumes while increasing OPD to 59.1 g atom L^{-1},
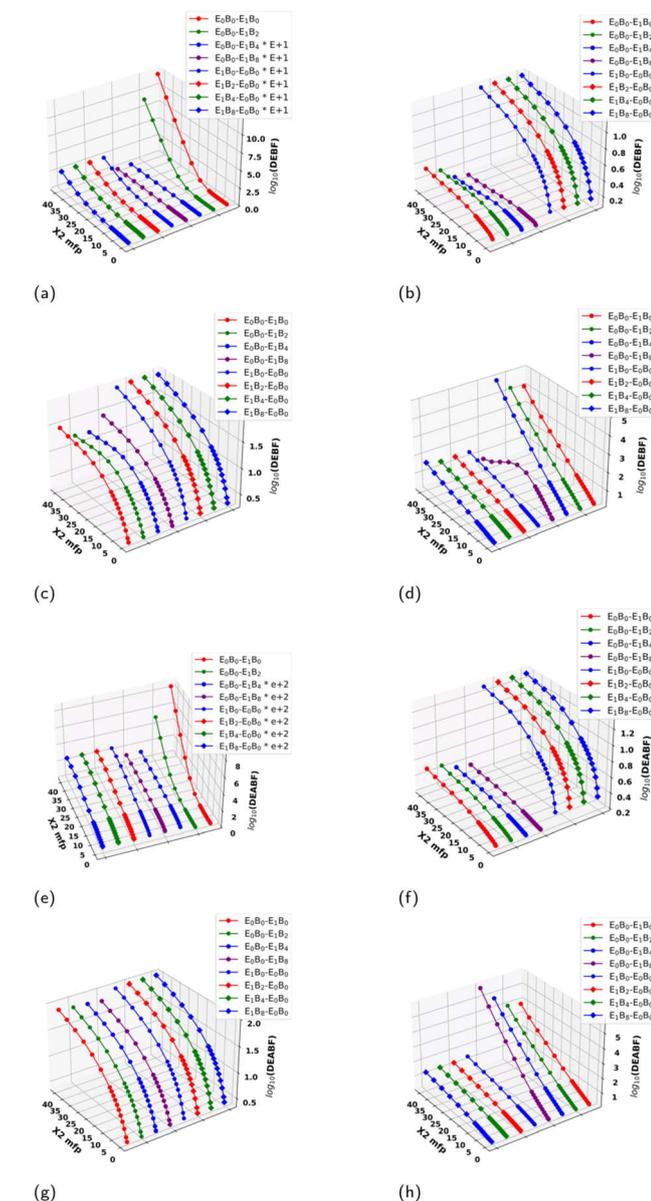

Fig. 9 Log$_{10}$ DLEBF versus penetration depth of DLE0 and DLE1 at selected photon energies of: (a) 0.015, (b) 0.15, (c) 1.5, and (d) 15 MeV. Log$_{10}$ DLEABF versus penetration depth of DLE0 and DLE1 at selected photon energies of: (e) 0.015, (f) 0.15, (g) 1.5, and (h) 15 MeV. Here, X_1 and X_2 indicate the penetration depth of the first and second layer, respectively.

confirming structure densification. LAC, MAC, σ-atomic, and σ-electron increased with higher Er_2O_3 and Bi_2O_3 content, while HVL and TVL decreased, enhancing shielding performance. E_1B_8 showed the highest γ-ray attenuation, and E_0B_0, as a second layer, provided superior multilayer absorption efficiency. Exposure buildup factors (EABF, DLEBF, and DLEABF) demonstrated strong dependence on photon energy and layer sequence. Nevertheless, excessive Bi_2O_3 (>4 mol%) caused phase separation and microcrack formation, as confirmed by SEM. The glass compositions containing 1 mol% Er_2O_3 and up to 4 mol% Bi_2O_3 exhibited optimal density, mechanical strength, and radiation shielding efficiency for medical and nuclear applications.

Author contributions

H. A. Abo-Mosallam & M. I. Abdelglil: synthesis of glass & mechanical study; E. E. Bayoumi: SEM-EDX, XRD analysis; A. M. A. El-Seidy: shielding/build-up shielding-factors & physical properties. H. A. Abo-Mosallam, M. I. Abdelglil, E. E. Bayoumi & A. M. A. El-Seidy: writing – review & editing, writing – original draft, validation, methodology, investigation, formal analysis, data curation, conceptualization.

Conflicts of interest

The authors declare that there is no conflict of interest.

Data availability

All data generated or analyzed during this study is included in this published article.

Supplementary information (SI): Fig. S1: EDX analysis of different phosphate glass samples: (a) E_0B_0, (b) E_1B_0, (c) E_1B_2, (d) E_1B_4. See DOI: https://doi.org/10.1039/d5ra07049j.

Notes and references

1 W. Martinez-López and M. P. Hande, Health effects of exposure to ionizing radiation, in *Adv. Secur. Safeguarding Nucl. Power Ind.*, Elsevier, 2020, pp. 81–97, DOI: 10.1016/B978-0-12-818256-7.00004-0.

2 R. Kurtulus, *Radiat. Phys. Chem.*, 2024, **220**, 111701.

3 W. Abd-Allah, S. Marzouk, M. Gaafar and E. Salama, *Ceram. Int.*, 2024, **50**, 46429–46439.

4 A. Paul Dhinakaran, P. Vinothkumar, S. Praveenkumar and M. Mohapatra, *Radiat. Phys. Chem.*, 2025, **226**, 112357.

5 M. Sayyed, A. Alshamari and M. Mhareb, *Radiat. Phys. Chem.*, 2025, **230**, 112565.

6 M. Elsafi, A. Hedaya and M. Sayyed, *Nucl. Eng. Technol.*, 2025, **57**, 103475.

7 E. A. Hussein, M. A. Barakat and N. R. Abd Elwahab, *J. Alloys Compd.*, 2024, **1008**, 176659.

8 J. Alyami, Y. Al-Hadeethi, O. A. Fallatah, S. Biradar, M. Sayyed and F. Almutairi, *Ann. Nucl. Energy*, 2025, **212**, 111069.

9 O. I. Sallam, Y. S. Rammah, I. M. Nabil and A. M. A. El-Seidy, *Sci. Rep.*, 2024, **14**, 1–17.

10 E. E. Bayoumi, M. O. Abd El-Magied, E. A. Elshehy, B. M. Atia, K. A. Mahmoud, L. H. Khalil and A. A. Mohamed, *Mater. Chem. Phys.*, 2022, **275**, 125262.

11 A. A. Al-Ghamdi, E. E. Bayoumi, S. Al-Farraj, M. Sillanpää and A. M. El-Seidy, *Surf. Interfaces*, 2025, **67**, 106567.

12 K. M. Kaky, M. Sayyed, M. K. Hamad, S. Biradar, M. Mhareb, U. Altimari and M. M. Taki, *Opt. Mater.*, 2024, **155**, 115853.

13 M. K. Hossain, G. A. Raihan, M. A. Akbar, M. H. Kabir Rubel, M. H. Ahmed, M. I. Khan, S. Hossain, S. K. Sen, M. I. E. Jalal and A. El-Denglawey, *ACS Appl. Electron. Mater.*, 2022, **4**, 3327–3353.

14 S. Erdönmez, *J. Adv. Res. Nat. Appl. Sci.*, 2025, **11**, 36–52.

15 A. S. Abouhaswa, U. Perişsanoglu, S. Saltık, N. Ekinci, M. H. Nasr, S. Kalecik and E. K. Perişsanoglu, *J. Inorg. Organomet. Polym. Mater.*, 2025, 4865–4883.

16 S. Yalcin, B. Aktas and D. Yilmaz, *Radiat. Phys. Chem.*, 2019, **160**, 83–88.

17 M. Al-Buriahi, N. Alomayrah, S. Owoeye and N. S. Alsaiari, *Radiat. Phys. Chem.*, 2025, **237**, 113042.

18 A. Makishima and J. Mackenzie, *J. Non-Cryst. Solids*, 1973, **12**, 35–45.

19 A. Abd El-Moneim, M. A. Azooz, H. A. Hashem, A. M. Fayad and R. L. Elwan, *Sci. Rep.*, 2023, **13**, 1–15.

20 A. Amat, H. M. Kamari, I. Mansor, N. Osman, N. N. S. Nidzam and N. I. M. Kamal, *Appl. Phys. A*, 2021, **127**, 792.

21 K. S. Mann and S. S. Mann, *Ann. Nucl. Energy*, 2021, **150**, 107845.

22 O. F. Ozpolat, B. Alım, E. Sakar, M. Büyükyıldız and M. Kurudirek, *Radiat. Environ. Biophys.*, 2020, **59**, 321–329.

23 P. Basu, R. Sarangapani and B. Venkatraman, *Appl. Radiat. Isot.*, 2019, **154**, 108864.

24 K. S. Mann, *Nucl. Eng. Technol.*, 2017, **49**, 792–800.

25 K. S. Mann, M. Kurudirek and G. Sidhu, *Appl. Radiat. Isot.*, 2012, **70**, 681–691.

26 J. Kaur, S. Kumar, I. Mudahar and K. Singh, *Mater. Chem. Phys.*, 2024, **314**, 128875.

27 M. M. Ismail, Y. M. Hamdy and E. A. Mahdy, *Opt. Mater.*, 2024, DOI: 10.2139/ssrn.4966373.

28 R. K. Guntu, M. Gopikrishna, S. Babu and M. Israr, *Ceram. Int.*, 2025, DOI: 10.1016/j.ceramint.2025.07.329.

29 M. Karabulut, A. Popa, G. Borodi and R. Stefan, *J. Mol. Struct.*, 2015, **1101**, 170–175.

30 K. Aly, H. Abo-Mosallam, E. A. Mahdy and M. M. Ebrahium, *Ceram. Int.*, 2025, **51**, 39390–39398.

31 F. Wang, Q. Liao, G. Xiang and S. Pan, *J. Mol. Struct.*, 2014, **1060**, 176–181.

32 H. Doweidar and Y. B. Saddeek, *J. Non-Cryst. Solids*, 2009, **355**, 348–354.

33 E. R. Shaaban, M. Shapaan and Y. B. Saddeek, *J. Phys.: Condens. Matter*, 2008, **20**, 155108.

34 M. Marzouk, H. ElBatal, A. Abdel Ghany and F. Ezz Eldin, *J. Mol. Struct.*, 2011, **997**, 94–102.

35 L. Koudelka, P. Mošner, M. Zeyer-Düsterer and C. Jäger, *J. Phys. Chem. Solids*, 2007, **68**, 638–644.

36 F. ElBatal, S. Ibrahim and A. Abdelghany, *J. Mol. Struct.*, 2012, **1030**, 107–112.

37 M. H. Wan, P. S. Wong, R. Hussin, H. O. Lintang and S. Endud, *J. Alloys Compd.*, 2014, **595**, 39–45.

38 Y. Chaitanya, S. Yusub, A. Ramesh Babu, V. Aruna, N. Sree Ram and C. Linga Raju, *Mater. Chem. Phys.*, 2022, **290**, 126584.

39 S. Thakur, V. Thakur, A. Kaur and L. Singh, *J. Non-Cryst. Solids*, 2019, **512**, 60–71.

40 A. A. Al-Ghamdi, A. A. Galhoum, A. Alshahrie, Y. A. Al-Turki, A. M. Al-Amri and S. Wageh, *Polymers*, 2022, **14**, 2568.

41 F. Assaf, A. El-Seidy, M. Abou-Krisha and A. Eissa, *Int. J. Electrochem. Sci.*, 2015, **10**, 5465–5478.

42 A. M. A. El-Seidy, M. S. El-Okaily, I. M. Nabil and A. A. Mostafa, *Sci. Rep.*, 2025, **15**, 13714.

43 Y. Shi, A. Tandia, B. Deng, S. R. Elliott and M. Bauchy, *Acta Mater.*, 2020, **195**, 252–262.

44 M. H. Alhakami, K. S. El-Nasser, N. A. Althubiti and T. A. M. Taha, *Nucl. Eng. Technol.*, 2026, **58**, 103925.

45 M. Gaafar, S. Marzouk, I. Mahmoud, H. Y. Amin, M. A. Hassan, A. Samir and H. Elsaghier, *Phys. B*, 2025, **707**, 417183.

46 G. Yang, G. Wenkai, Z. Kang, X. Wu, Y. Hou, J. Cui, X. Li, S. Zhang, Y. Yunlong and J. Kang, *J. Non-Cryst. Solids:X*, 2025, DOI: 10.2139/ssrn.5098464.

47 A. Masuno, Y. Mikami, Y. Yanaba, Y. Higo, S. Sasaki, I. Sato, T. Yaji, G. A. Rosales-Sosa and H. Inoue, *Acta Mater.*, 2025, **283**, 120549.

48 F. H. Assaf, M. M. Abou-Krisha, O. k. Alduaij, A. M. El-Seidy and A. A. Eissa, *Int. J. Electrochem. Sci.*, 2015, **10**, 6273–6287.

49 M. Ahmadi, Z. Vahid and N. Darush, *Radiat. Phys. Chem.*, 2024, **217**, 111450.

50 B. Aktas, S. Yalcin, M. Albaskara, E. Aytar, G. Ceyhan and Z. S. Turhan, *J. Non-Cryst. Solids*, 2022, **584**, 121516.

51 A. M. El-Seidy, M. A. Elbaset, F. A. Ibrahim, S. A. Abdelmottaleb Moussa and S. A. Bashandy, *J. Trace Elem. Med. Biol.*, 2023, **80**, 127312.

52 M. Laourayed, Y. Alaoui, A. Er-rafai, M. El Mouzahim, M. El Moudane, M. Abid, M. Beraich, A. Guenbour and A. Bellaouchou, *EPJ. Applied physics*, 2022, **97**, 49.

53 S. Damodaraiah, V. Reddy Prasad and Y. Ratnakaram, *Spectrochim. Acta, Part A*, 2017, **181**, 264–269.

54 M. Abd Elwanees, *Mat. J. Vet. Med.*, 2023, **3**, 50–57.

55 A. Acikgoz, G. Demircan, D. Yılmaz, B. Aktas, S. Yalcin and N. Yorulmaz, *Mater. Sci. Eng., B*, 2022, **276**, 115519.

56 N. A. Alsaif, N. Alfryyan, H. Al-Ghamdi, Y. Rammah, E. A. Mahdy, H. Abo-Mosallam and F. El-Agawany, *Opt. Mater.*, 2024, **157**, 116081.

57 a. elseidy, S. Bashandy, F. Ibrahim, S. Abd El-Rahman, O. Farid, S. Moussa and M. El-Baset, *Egypt. J. Chem.*, 2022, **65**, 497–511.

58 A. M. A. El-Seidy, O. I. Sallam, I. M. Nabil, Y. S. Rammah, M. S. El-Okaily and H. Alshater, *Sci. Rep.*, 2024, **14**, 1–21.

59 N. A. M. Alsaif, N. Alfryyan, H. Al-Ghamdi, A. M. A. El-Seidy, A. M. Abdelghany, Y. S. Rammah and A. S. Abouhaswa, *J. Inorg. Organomet. Polym. Mater.*, 2024, **34**, 3623–3631.

60 I. M. Nabil, A. M. A. El-Seidy, A. T. Mosleh, H. Y. Zahran, S. H. Zyoud and I. S. Yahia, *J. Mater. Sci.: Mater. Electron.*, 2024, **35**, 1329.

61 M. A. E. M. Sayed, N. A. A. E. Latif, F. A. H. A. S. Ibrahim, A. M. A. El-Seidy, S. A. A. Moussa and S. A. E. M. Bashandy, *Braz. Arch. Biol. Technol.*, 2024, **67**, 1–15.

62 S. A. E. Bashandy, A. M. A. El-Seidy, F. A. A. Ibrahim, S. S. Abdelrahman, S. A. Abdelmottaleb Moussa and M. A. ElBaset, *Sci. Rep.*, 2023, **13**, 1–20.

63 M. S. El-Okaily, A. M. A. El-Seidy, E. H. Ismail, R. M. Allam, A. A. Saeed, A. Bhaumik and A. A. Mostafa, *J. Mater. Res.*, 2024, **39**, 1741–1757.

64 S. A. E. Bashandy, M. A. Elbaset, F. A. A. Ibrahim, S. S. Abdelrahman, S. A. A. Moussa and A. M. A. El-Seidy, *Sci. Rep.*, 2025, **15**, 1–19.

65 A. M. A. El-Seidy, I. E. El-Sayed, M. Linnolahti, E. E. Bayoumi, H. I. Mira and A. A. Galhoum, *RSC Adv.*, 2025, **15**, 28269–28279.

66 G. A. Alharshan, A. M. A. El-Seidy, M. I. Elamy, I. M. Nabil, A. M. El-Refaey, R. A. Elsad, M. S. Shams, A. M. Abdelghany and Y. S. Rammah, *J. Mater. Sci.: Mater. Electron.*, 2024, **35**, 862.